The effect of pressure on radiative losses in hot, warm, and cool microgravity spherical diffusion flames

Kendyl A. Waddell[a,*], Daniel L. Dietrich[a], Vedha Nayagam[b]

[a] *NASA Glenn Research Center, Cleveland, OH, 44135, USA*
[b] *Department of Mechanical and Aerospace Engineering, Case Western Reserve University, Cleveland, OH 44106, USA*

Abstract
This work investigates the effects of ambient pressure on radiative heat losses in hot, warm, and cool microgravity spherical diffusion flames using a numerical model and compares the results to observations from microgravity experiments. The experimental data was obtained during droplet combustion experiments, and the numerical model simulates burner-supported flames. The similarities in the gas phase between the two configurations allow these simulations to provide accurate insights into the experimental results. The model uses a statistical narrow-band model that includes emission and reabsorption. The effect as pressure was varied between 0.5 and 10 atm on the relative radiation contributions from CO_2 and H_2O, the primary radiating species, was examined. As the pressure increased H_2O contributed more to radiative loss than CO_2 in both the experiments and computations. This was determined to be caused by increased absorption coefficients leading to increased reabsorption at higher pressures. Calculations performed without reabsorption did not see this effect, confirming it is due to the optically thick nature of the system. Reabsorption was higher for CO_2 due to the prominence of the absorption band at 4.3 μm, which became saturated at higher pressures. These results demonstrated the importance of using the optically thick assumption to accurately account for radiative losses in these flames, which are crucial to capture flame behaviours such as radiative extinction and reignitions.

Keywords: Radiative heat loss; Optical thickness; Cool flames; Warm flames; Microgravity

*Corresponding author.

Novelty and significance statement

The novelty of this study is that it provides the first comprehensive analysis of the effects of pressure on radiative reabsorption in hot, warm, and cool microgravity diffusion flames. A statistical narrow band radiation model is used to explain previously unexplained experimental behaviour from International Space Station droplet combustion experiments, where the contribution to total radiative loss shifted from CO_2 dominated to H_2O dominated at higher pressures. The results show for the first time this behaviour was caused by the saturation of CO_2 absorption bands and could not be accounted for with optically thin radiation models. This demonstrates the limitations of using the optically thin assumption when calculating radiative loss in combustion systems, particularly at elevated pressures, which has significant implications for flame stability, extinction, and reignition.

1. Introduction

Radiative heat transfer is of great importance in many combustion systems, particularly in high temperature systems such as flames and fires where it can be the dominant mode of heat transfer. In microgravity, where natural convection is eliminated, combustion products accumulate in the flame region and radiate heat while the chemical heat release from the flame remains relatively constant, causing the flame temperature to decrease until combustion can no longer be sustained. This phenomenon, known as radiative extinction, has been the subject of several previous studies [1–5]. Most studies are primarily concerned with the total radiative loss from the flame, and less so with the individual contributions from different species. The primary radiating species in combustion systems are H_2O, CO_2, CO, soot, and fuel vapor. Often CO_2 and H_2O are the main contributors to radiative heat loss.

Radiative heat transfer in combustion systems has been studied extensively, with particular attention paid to the accuracy of different radiation property models and radiative transfer equation (RTE) solution methods [6–11]. The main types of radiation models, in order of increasing accuracy, are grey gas, wide band, narrow-band, and line-by-line models. Grey gas models do not account for the change of radiative properties with wavelength and tend to result in unacceptable accuracy. Wide band models divide the

absorption and emission spectra into a few wide bands and are computationally inexpensive but still not of high enough fidelity for most combustion applications. Narrow band models divide the spectral domain into even smaller bands and average the absorption coefficient over each band. With small enough bands, this method can produce comparable results to the line-by-line model while greatly reducing computational time. Line-by-line models consider each spectral line individually and are highly accurate but often too computationally expensive. In general, the statistical narrow band (SNB) method strikes a good balance between accuracy and computational time [7,9,12–14] for detailed simulations of laboratory-scale flames.

When solving the RTE it is common to use one of two treatments. The first is that radiators both emit and absorb radiation, i.e., the system is optically thick. This is the more accurate treatment but greatly increases computation time. The second treatment is to assume radiators only emit radiation but do not absorb it, i.e., the system is optically thin. This can greatly reduce computation times but is often unable to reproduce experimental behavior without additional correction factors [6–11].

There have been studies that examined the effects of using the optically thin or optically thick assumption, [9,11] or the effects of changing stretch rate [10,12] or ambient pressure [14], which affect the optical thickness [10,12,14] on radiative heat transfer. Bedir et al. [9] compared different radiation models for a PMMA stagnation point flame. They found that using the SNB model with the optically thin assumption overpredicted radiative emission by as much as 57%, and similar results were obtained using the Planck mean absorption coefficient. Applying a factor of 0.44 to the Planck mean results provided good agreement with the total emission from the optically thick narrow band calculations, but there were still inaccuracies in the distribution of radiation.

Ju et al. [11] calculated new Planck mean absorption coefficients using the SNB model and compared the resulting heat fluxes to those obtained from the SNB method for a counterflow CH4 flame. They found that the Planck mean absorption coefficient overpredicted radiative heat loss due to the lack of radiation reabsorption. Rhatigan et al. [12] used an SNB model to calculate the radiation heat transfer in a PMMA stagnation point diffusion flame and compared the results to using the Planck mean absorption coefficient and the optically thin SNB model. They found that the Planck mean and optically thin SNB methods both overpredicted emission due to a lack of absorption, and that the net radiative loss from the flame increased with increasing stretch rate. Chu et al. [14] studied the effects of total pressure on radiative heat transfer in a parallel plate geometry containing CO_2, H_2O, and mixtures of the two. They showed that radiative emission and absorption increased with increasing pressure due to increasing optical thickness but did not differentiate between CO_2 and H_2O emission/absorption.

Bedir and T'ien [10] studied radiation in a PMMA stagnation point diffusion flame at varying stretch rates. They considered the radiation emission and absorption contributions for CO_2, H_2O, and fuel vapor. As the stretch rate increased the optical thickness of the system decreased due to the pressure path length of the radiating species decreasing. Most of the emitted radiation came from CO_2, and the contribution to total emitted radiation from CO_2 increased with increasing optical thickness. As optical thickness increased the absorption percentage of gas phase radiation increased for both CO_2 and H_2O, but the CO_2 increase was much larger. Most of the absorption was determined to be self-absorption, i.e., radiation from a particular species was absorbed by that same species, rather than cross absorption.

Both droplet [1,3,8,15,16] and burner supported [2,5,17–20] configurations are commonly used to study microgravity spherical diffusion flames experimentally and numerically. The two configurations are similar, differing primarily by the boundary conditions at the surface of the droplet or sphere. The burner-supported configuration is, however, computationally easier (faster) to study since the mass flux and temperature at the burner surface are prescribed rather than being part of the solution. Both microgravity droplet and burner-supported combustion experiments have a gas-phase that can be considered quasi-steady outside of the ignition and extinction transients. This allows the burner-supported configuration to provide accurate insights into the gas-phase processes [3,4,20], provided the boundary conditions at the burner surface match the burning rate and droplet surface temperature in the experiment.

Warm and cool diffusion flames are relatively new areas of study. Cool diffusion flames were first observed during droplet experiments on the International Space Station (ISS) in 2012 [21], and warm diffusion flames were first observed in normal gravity counterflow experiments [22] and microgravity droplet experiments [23] in 2018. These flames burn at lower temperatures than typical hot flames and follow different chemical kinetic pathways. Understanding their behavior is key to developing advanced engine technologies that utilize their chemistry to create engines that are more efficient and less polluting. These flames can also exist outside the typical flammability limits of hot flames and are favored to form in microgravity, making them important to both terrestrial and spacecraft fire safety. Compared to hot flames, there has been little research into the radiative properties of these flames. Lin et al. [24] modeled thermal radiation in counterflow warm and cool diffusion flames but used an optically thin radiation model due to short optical lengths in that configuration. They found that thermal radiation did affect the flammability limits of the flames. Farouk et al. [23] modeled radiation in

microgravity droplet diffusion flames using an SNB model and found that total radiative losses were lower during the warm and cool flame burning periods compared to the hot flame but did not consider the relative contributions from individual species.

During recent droplet experiments performed aboard the ISS radiance measurements were taken that captured both the total flame radiance and the radiance from water vapor in the 5-7 μm range at various ambient pressures [16]. A trend observed during these experiments was that, during the hot flame, as ambient pressure increased and as the flame burned the fraction of total radiation that came from water vapor increased. This trend could not be easily explained, as the production rates of main radiators CO_2 and H_2O should be relatively constant between conditions, and any changes to product formation should affect both radiators equally. The objective of this work is to use a transient numerical model of burner supported flames with an optically thick SNB model to recreate and determine the cause of the experimental behavior. The influence of using the optically thick or optically thin assumption on the accuracy of the numerical predictions is also examined for the spherically symmetric diffusion flames.

2. Methods

2.1 Experimental

Droplet experiments were carried out aboard the ISS as part of the Cool Flames Investigation (CFI), a subset of the Flame Extinguishment Experiment (FLEX) set of experiments. More details on the experiments can be found in [15,16,25,26]. Both free floated droplets and droplets supported by a 40 μm carbide fiber were examined, and initial droplet diameters for the pure dodecane experiments ranged from 4 to 4.5 mm. The ambient was air (0.21/0.79 O_2/N_2) for most of the tests and the ambient pressure ranged from 0.5 to 5 atm.

The droplet and flame were monitored using color, backlit, and intensified cameras. Droplet sizes were measured using the backlit camera, and the estimated uncertainties in droplet size are ± 50 μm [15].

Flame radiance was measured by two radiometers, one wideband and one narrowband, both located 110 mm away from the droplet deployment site. The wideband detector was a silicon-based thermopile detector with a KRS-5 window that limited the spectral response from 0.58 μm to 50 μm, used argon as a back-fill gas, had an active area of 0.36 mm^2, and was preceded by an aperture with a diameter of 3.175 mm. The narrowband detector was a thin-film based thermopile with a silicon long-wave-pass filter and sapphire window that limited the spectral range from 5 μm to 7 μm, where water vapor exhibits strong absorbance. It used xenon as a back-fill gas, had an active area of 4.0 mm^2, and was preceded by an aperture with a diameter of 4.572 mm [15].

The radiometers were calibrated using a calibrated blackbody source, and total radiance was determined using this calibration and details of the radiometer geometry relative to the droplet and flame. Uncertainties in flame radiance are estimated to be up to ± 20% [15]. More details on the radiometers and their calibration, as well as the conversion from irradiance to flame radiance, can be found in [15].

2.2 Numerical

Numerical simulations were performed using the SphDiff program [18–20,27,28], which is a modification of Sandia PREMIX and uses the Chemkin-II package [29]. This numerical model has been used in various studies of burner supported spherical diffusion flames and has been shown to accurately reproduce the experimental results [18–20,27,28]. A full model description can be found in [20,27,28].

The inner boundary was the burner surface, at a radius of 2.25 mm. Mass flow rate and burner temperature were prescribed, and species mass flux and energy were conserved. The outer boundary was at a radius of 100 cm and temperature and species concentrations were prescribed there. The domain was sufficiently large that there was no change in species or temperature near the outer boundary.

An adaptive grid algorithm was used, as in [20]. The domain was divided into three grid areas: an inner area, a reaction area, and an outer area. The inner area follows the same algorithm as [28], and the reaction area has 200 grid cells with 0.001 cm spacing and was centered about the peak temperature. From there, the grid spacing in the outer area increased by 5% for each grid cell moving outward. A total of 373 grid cells were used, which satisfied grid independence.

The radiation model is described in detail in [27,28]. The model considered radiation heat loss from CO, CO_2, and H_2O. A detailed absorption/emission statistical narrow band model was used to calculate the absorption coefficient for these species. For optically thin simulations, absorption was neglected. Radiation properties were taken from the HITRAN database [30] with wavenumbers ranging from 150 to 9300 cm^{-1}. The data was divided into 366 bands, each of 25 cm^{-1}, and properties were averaged over each band considering a Lorentz spectral line shape of random spacing and strength. The radiative transfer equation was solved using a discrete-ordinates method [27,28]. Radiation from soot was not considered in these simulations, as experimental observations show luminous soot does not typically form in these flames after the ignition transient owing to the large radiative losses reducing the temperature below the sooting threshold [3,4,20].

For the simulations the fuel was pure heptane, owing to the lack of an available dodecane chemical kinetic mechanism that was compatible with SphDiff. The radiative extinction characteristics of the dodecane droplets were very similar to those for pure

heptane droplets so the fuel choice has minimal impact on the results. It was shown in a previous study that flame radiance for different hydrocarbons was similar despite their different compositions [15]. Thus, it is reasonable to compare the results of heptane simulations to those of dodecane experiments. The chemical kinetics mechanism from UCSD, which has 65 species and 303 reactions, was used [31]. As in the experiments, the ambient was air (0.21/0.79 O_2/N_2). Mass flow rate was held constant at 0.9 mg/s, this value was chosen to closely match the experimentally measured burning rate constants. The burner surface temperature was held constant at the boiling point of heptane at each pressure, and pressure was varied from 0.5 to 10 atm. The burner size, temperature, and mass flow rate were chosen to best replicate the conditions from the droplet experiments.

3. Results and Discussion

Figure 1a shows the simulated temporal evolution of flame temperature and flame radius for the 1 atm, 4 atm, and 10 atm cases. These simulations were performed using the SNB method with emission and reabsorption. The flames ignite at temperatures above 2000 K, after which the peak temperature decreases due to increasing radiative losses. As the flame temperature decreases it is possible for the flame to traverse all three combustion regimes, hot, warm, and cool flames, depending on the pressure.

As hot flame peak temperature reaches ~1200 K, the hot flame either radiatively extinguishes if the pressure is less than 4 atm or transitions to a warm flame if the pressure is 4 atm or higher. In the cases where a warm flame is established, the transition from hot flame to warm flame is not obvious when looking at the temperature or radius curves. Once a warm flame is established it burns in a similar manner to a hot flame and radiatively extinguishes before a cool flame is established. This section is organized such that the combustion regimes are discussed separately, starting with the hot flame, and moving to the warm flame and then the cool flame.

3.1 Hot Flame

Figure 1a shows that the evolution of flame temperature is nearly invariant with pressure during the hot flame. Peak temperature is controlled by the balance between radiative loss and chemical heat release, both of which decrease with increasing pressure due to the increasing influence of intermediate-temperature HO_2 chemistry, which shifts chemical pathways and has a weakening effect on the hot flame [32]. Also shown in Fig. 1a is the flame radius, which decreases with increasing pressure. Increased pressure decreases the flow velocity and increases the molar density of fuel vapor and oxidizer in the system, allowing the flame to establish at locations closer to the burner surface.

The net molar production rate of the radiating products H_2O, CO_2, and CO are shown in Fig. 1b.

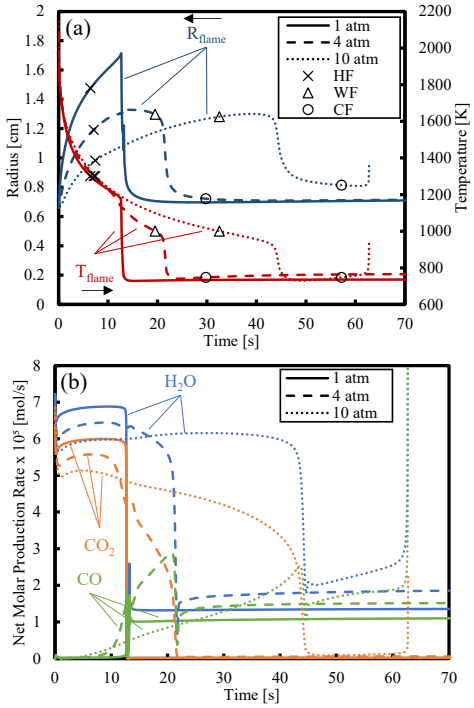


Figure 1: Temporal evolution of (a) flame temperature and flame radius and (b) H_2O, CO_2, and CO production at 1 atm, 4 atm, and 10 atm. (a) Symbols indicate points in the hot flame (HF: T = 1300K), warm flame (WF: T = 1000 K) and cool flame (CF: T = 750 K) to be examined in more detail.

During the hot flame H_2O is produced at higher rates than CO_2, consistent with the stoichiometry, and the production of both is relatively steady with time and decreases with increasing pressure, due to the rise pressure-dependent intermediate-temperature HO_2 chemistry [32]. There is little to no CO production during the hot flame.

The simulated temporal evolution of H_2O, CO_2, and CO radiance, integrated across the entire computational domain at each timestep, for the 1 atm, 4 atm, and 10 atm cases is shown in Fig. 2. Figure 2a shows the raw computed values; in Fig. 2b they are normalized by the flame diameter cubed at each timestep to account for size effects.

During the hot flame all the radiance comes from H_2O and CO_2. Water vapor radiance increases with increasing time at all pressures due to flame growth, when this is accounted for H_2O radiance decreases as time increases. In Fig. 2a CO_2 radiance is relatively constant with time following the initial ignition transient. When flame size is accounted for CO_2 radiance decreases with increasing time, and the degree of this decrease is higher than that for H_2O.

Water vapor radiance increases with increasing pressure in the hot flame, while CO_2 radiance decreases with increasing pressure. When flame size is taken into consideration that radiance from both species increases with increasing pressure, though

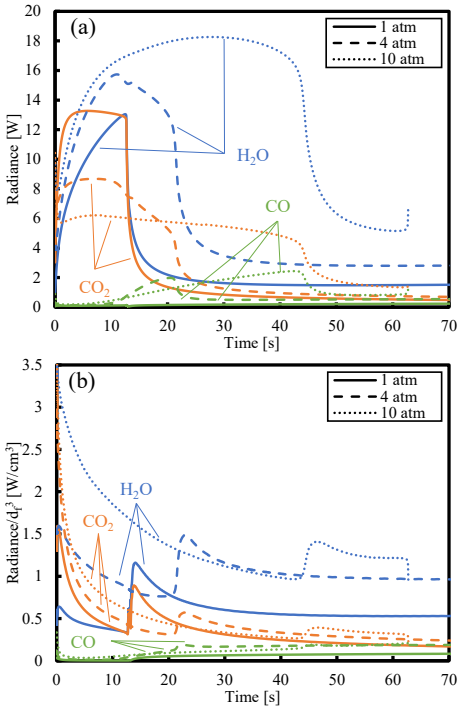


Figure 2: Temporal evolution of radiative losses from H_2O, CO_2, and CO for the 1 atm, 4 atm, and 10 atm cases. (a) Integrated radiance, (b) integrated radiance normalized by flame diameter cubed.

H_2O increases to a larger extent. Since the changes in production rate with pressure affect both species in the same direction, the only explanation for a difference in their behavior is a difference in the radiative properties for each species.

Both as the flame burns and as pressure increases, the absorption coefficients of H_2O and CO_2 increase due to increasing molar concentrations. Increased absorption coefficients lead to higher emission and reabsorption of radiation. With the optically thin assumption there is no reabsorption of radiation, and comparing optically thin calculations to optically thick calculations isolates the reabsorption effects. The radiation calculations were re-performed using the same temperature and species profiles that were obtained with optically thick simulations, but neglecting the reabsorption term from the RTE. The reabsorption fraction is then calculated as $1-R_{thick}/R_{thin}$, where R is the total radiance. The resulting reabsorption fraction (i.e., the fraction of emitted radiation that was reabsorbed) is shown in Fig. 3.

A low reabsorption fraction indicates that most of the emitted radiation escapes the system, and there is little reabsorption, while a high reabsorption fraction indicates most of the emitted radiation is reabsorbed before it leaves the system. The reabsorption fraction shows that CO_2 reabsorption is significantly higher than H_2O reabsorption during the hot flame at all pressures, and both values increase with increasing

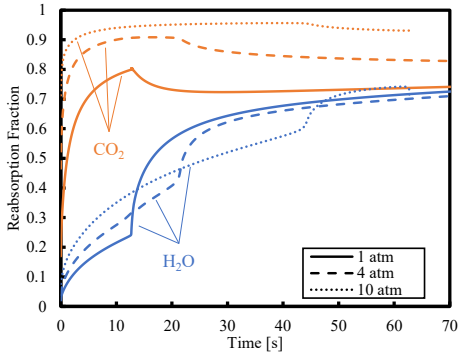


Figure 3: Temporal evolution of H_2O and CO_2 reabsorption fractions for the 1 atm, 4 atm, and 10 atm cases.

pressure. This explains the trends seen in Fig. 2. Radiance from CO_2 is relatively constant with time because early in the flame lifetime a high percentage of the emitted radiation is reabsorbed. Meanwhile H_2O reabsorption levels are low, and as such H_2O radiance can continually increase with time. The same is true as pressure increases, CO_2 reabsorption is so high that its radiance decreases with increasing pressure, while H_2O reabsorption is low enough that its radiance can increase as pressure increases.

The radiance values shown in Fig. 2 for each species were obtained by integrating the radiance from the surface to the outer boundary, which is the equivalent of the total radiative loss from the system. If the integration is instead performed from the surface to some intermediate radius, the result is the radiative loss from the system up to that radius, which is the equivalent of placing a radiometer at that point. Figure 4 shows this integration for the 1 atm and 4 atm cases when the peak temperature is 1300 K, considering both optically thick and optically thin calculations. The distribution of temperature is also shown.

Considering CO_2 in the optically thick cases, moving outwards from the burner surface, there is a region of net reabsorption near the burner surface, after which radiance increases sharply in the high temperature region near the flame. The radiance then peaks and begins to decrease due to reabsorption by the large concentration of accumulated products at low temperature in this region and finally plateaus as the temperature and species concentrations decrease. For H_2O the distribution is similar, but the effect of reabsorption is less pronounced. These trends are the same between the 1 atm and 4 atm cases, with the 4 atm case having a more compressed profile.

When reabsorption is neglected, radiance from both H_2O and CO_2 increases continually throughout the flame region until there are no more radiating products. There is a much more significant difference between the optically thick and optically thin cases for CO_2 than H_2O, owing to higher levels of reabsorption.

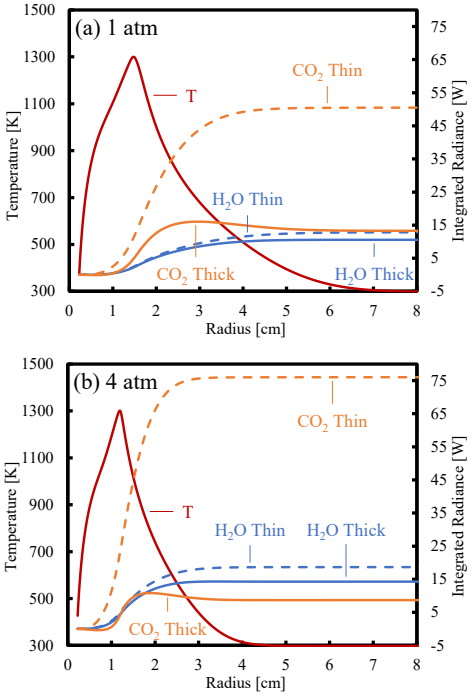


Figure 4: Temperature distributions and H_2O and CO_2 integrated radiance distributions with and without reabsorption for the (a) 1 atm and (b) 4 atm cases when the peak temperature was 1300 K.

The differences in reabsorption are due to the spectral properties of each species. Figure 5 shows the absorption cross sections of H_2O and CO_2 at 750 K and 1500 K, obtained from the HITRAN database [30]. These values are multiplied by Avogadro's number and the molar concentration to obtain absorption coefficient. The H_2O absorption spectrum is broad, while the CO_2 spectrum has strong peaks centered at 4.3 µm and 15 µm. When temperature increases the shape of the H_2O spectrum changes slightly, with its magnitude decreasing at some wavelengths and increasing at others. The CO_2 spectrum keeps the same general shape as temperature increases, and the magnitude of its peaks decreases. The 4.3 µm band has the highest magnitude and is the key to understanding the difference in reabsorption behaviors between the two molecules.

Increasing pressure while holding other conditions constant increases the molecular density of the system, which increases absorption coefficient. A high absorption coefficient indicates that radiation is likely to be reabsorbed before it escapes the region where it is emitted, with total radiative intensity limited by the Planck blackbody function. When the absorption coefficient is initially low, the intensity is far away from this limit and can increase towards it as absorption coefficient increases. When the absorption coefficient is initially high, as it is in the 4.3 µm band for CO_2, total intensity in that band is already near the limit and any new emission is almost immediately reabsorbed.

This can be seen in Figure 6, where the radiance distribution across the domain has been broken down according to wavelength for the 1 atm case (with and without reabsorption) and the 4 atm case (with reabsorption) when the peak temperature is 1300 K. Neglecting reabsorption in the 1 atm case increases radiance by a fair amount across the H_2O spectrum and in the 15 µm band for CO_2. In the 4.3 µm band the amount of reabsorption is much higher, 80% of the CO_2 radiance in that band is reabsorbed. There is a moderate increase in the radiance values in the 4 atm case compared to the 1 atm case across the H_2O spectrum and in the 15 µm band for CO_2, but in the 4.3 µm band the radiance mostly decreased as pressure increased.

Figure 7 summarizes the changes in H_2O and CO_2 radiance during the hot flame as pressure changes from 0.5 to 10 atm for cases with and without reabsorption. Figure 7a shows the H_2O and CO_2 radiance when the flame temperature is 1300 K at each pressure, normalized by the flame diameter cubed to remove flame size effects. Water vapor radiance increases with increasing pressure both with and without reabsorption, and the increase for cases without reabsorption is more significant. The same is true for CO_2 to an even larger extent, optically thick CO_2 radiance increases only slightly with increasing pressure, and optically thin radiance is an order of magnitude higher at higher pressures. Such a high amount of reabsorption is due to saturation of the 4.3 µm CO_2 band, keeping CO_2 radiance nearly level as pressure increases.

Figure 7b shows how the fraction of total radiance that comes from CO_2 and H_2O (the radiance ratio) changes as pressure increases for cases both with and without radiation reabsorption. In cases without reabsorption the radiance is consistently around 0.8 for CO_2 and 0.2 for H_2O, as the radiance for both increases linearly with pressure. However, in cases with reabsorption CO_2 radiance dominates at lower pressures, and as pressure increases the CO_2 radiance ratio decreases and more of the radiance comes from H_2O. This same behavior was also observed in microgravity droplet experiments [16] and is caused by H_2O radiance increasing as pressure increases while CO_2 radiance remains nearly constant.

3.2 Warm Flame

Warm flames were only established when the pressure was 4 atm or higher. Unlike in the hot flame, in the warm flame the evolution of peak temperature with time changes with pressure. Temperature decreases more quickly in lower pressure hot flames, as seen in Fig. 1a, because the intermediate-temperature chemistry that supports these flames is stronger at higher pressures [32].

Fig. 1b shows that during the warm flame H_2O is produced at similar levels to its production in the hot

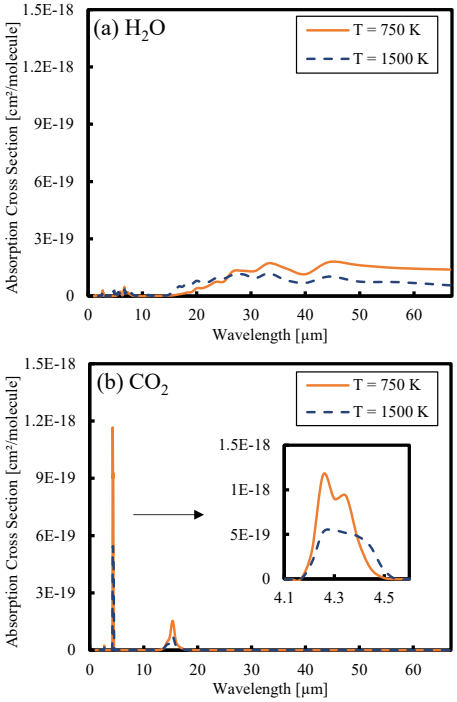


Figure 5: (a) H_2O and (b) CO_2 absorption cross sections from the HITRAN database vs. wavelength at temperatures of 750 K and 1500 K.

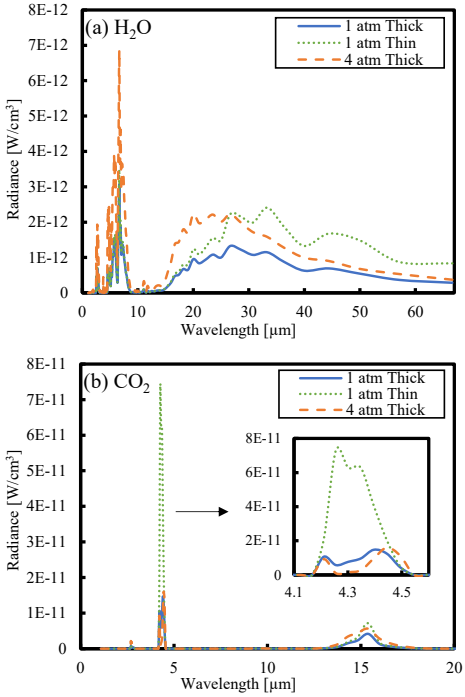


Figure 6: (a) H_2O and (b) CO_2 integrated radiance vs wavelength for the 1 atm and 4 atm cases when the peak temperature was 1300 K.

flame, decreasing slightly at 4 atm and increasing slightly at 10 atm. The production of CO_2 decreases in the warm flame compared to the hot flame, and the corresponding CO production increases as there is less conversion from CO to CO_2 in the warm flame. CO_2 production continues to decrease as time goes on in the warm flame, with CO production increasing. As pressure increases the production of CO_2 and H_2O increase, while the production of CO decreases.

Despite the increase in CO production during the warm flame, it still only contributes a small fraction of the total flame radiance, as seen in Fig. 2. The main radiators are still CO_2 and H_2O, with H_2O constituting most of the radiance. Radiance from CO peaks just before warm flame radiative extinction. Figure 2b shows that when accounting for flame size CO_2 and H_2O radiance continue to decrease with increasing time in the warm flame.

To examine the effect of increasing pressure on the warm flame, the point where the peak temperature was 1000 K was chosen for comparison. Since the rate of temperature decrease decreases with increasing pressure in the warm flame, the flame takes longer to reach this temperature at higher pressures. Figure 8 summarizes the results from the warm flames when the peak temperature is 1000 K as pressure increases from 4 atm to 10 atm. Fig. 8a shows the radiance from H_2O and CO_2 divided by the flame diameter cubed, and Fig. 8b shows the radiance ratio for these species, for cases both with and without reabsorption. The results here are much like the higher-pressure results for the hot flame shown in Fig. 7. Reabsorption from CO_2 is high enough that its radiance is constant with changing pressure when reabsorption is included, while the radiance from H_2O increases slightly with increasing pressure. In the optically thin cases the radiance from both species increases with increasing pressure, as the molar concentrations are higher due to the increased pressure and longer burning durations.

Most of the radiance comes from H_2O at all pressures during the warm flame for the optically thick calculations. The radiance ratio values for the optically thin cases are the mirror image of the optically thick cases, with most of the radiance coming from CO_2 at each pressure. The difference in spectral properties that caused the trends observed in the hot flame are also responsible for the results here. In the warm flame the reabsorption coefficient is even higher due to decreasing peak temperatures and increasing product concentrations, causing the CO_2 reabsorption fraction to peak during the warm flame as shown in Fig. 3.

3.3 Cool Flame

Once the cool flame is established its burning behavior changes depending on the ambient pressure, as seen in Fig. 1a. For cool flames at pressures of 4 atm and below, there is a period after the cool flame is established where the peak temperature increases

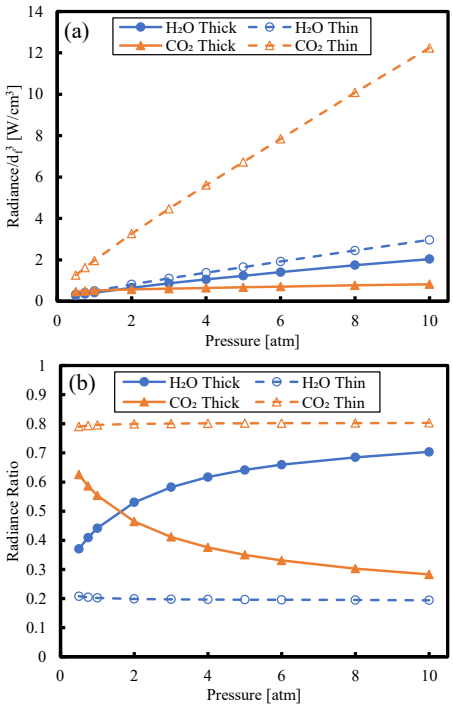


Figure 7: (a) Hot flame H_2O and CO_2 integrated radiance normalized by flame diameter cubed and (b) hot flame H_2O and CO_2 radiance ratio, as pressure increases from 1 atm to 10 atm. The flame temperature was 1300 K, and calculations with and without reabsorption of radiation are shown.

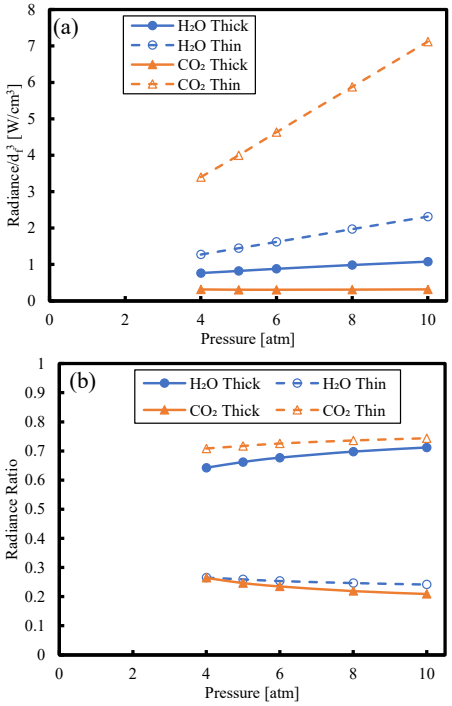


Figure 8: (a) Warm flame H_2O and CO_2 integrated radiance normalized by flame diameter cubed and (b) warm flame H_2O and CO_2 radiance ratio, as pressure increases from 4 atm to 10 atm. The flame temperature was 1000 K, and calculations with and without reabsorption of radiation are shown.

with time, before peaking and decreasing towards a steady-state value. When the pressure is 5 atm and higher, the temperature increase at the beginning of the cool flame is enough to make it reignite back to a hot flame. The reignition is due to pressure dependent intermediate-temperature HO_2 chemistry, which provides additional heat release in the cool flame [32].

Figure 1b shows that H_2O production drops significantly in the cool flame compared to the hot/warm flame, as does CO_2, to the point that there is little to no CO_2 production. The production of CO is higher than it is in the hot flame, but lower than the peak level reached in the warm flame if a warm flame was present. The production rates of H_2O and CO are comparable, with H_2O being slightly higher, and the production of all three species increases with increasing pressure.

Figure 2a shows that, at all pressures, radiance from CO_2 and H_2O drops significantly in the cool flame compared to the hot and warm flames. However, Fig. 2b shows that when flame size is accounted for there is a sharp increase in radiance as the cool flame forms due to the sharp decrease in flame radius between the hot/warm flames and the cool flame. The result is that the flame size adjusted radiance is higher in the cool flame than the later points in the hot and warm flames.

Figure 2 shows that the radiance in the cool flame mostly comes from H_2O. The rest of the radiance mostly comes from CO_2, with a smaller contribution from CO, despite the lack of CO_2 production. Besides the small amount of CO_2 production there is still residual CO_2 from the hot/warm flame, and CO_2 is a much stronger radiator than CO.

The point where the cool flames had a peak temperature of 750 K was chosen for comparison, and summary plots for the cool flames at 750 K from 2 atm to 10 atm are shown in Fig. 9. The cases at 1 atm and below do not reach this temperature and are not included.

The radiance from H_2O and CO_2 divided by the flame diameter cubed is shown in Fig. 9a. For the cases with reabsorption the radiance from H_2O is consistently higher than that from CO_2 at both pressures. This holds true for the 2 atm case when reabsorption is neglected, but as the pressure increases the radiance from CO_2 and H_2O are nearly equal when reabsorption is not included. The jump in CO_2 radiance between 2 atm and 3 atm is because the 2 atm case takes longer to reach 750 K than the 3 atm and higher cases. Since there is little CO_2 production in the cool flame, in the early cool flame residual CO_2 concentration in the flame region is high from the hot/warm flame, and it decreases as the CO_2 diffuses

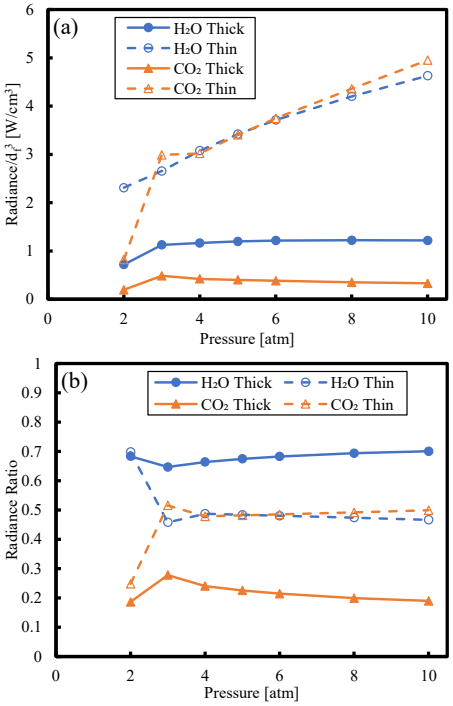


Figure 9: (a) Cool flame H_2O and CO_2 integrated radiance normalized by flame diameter cubed and (b) cool flame H_2O and CO_2 radiance ratio, as pressure increases from 2 atm to 10 atm. The flame temperature was 750 K, and calculations with and without reabsorption of radiation are shown.

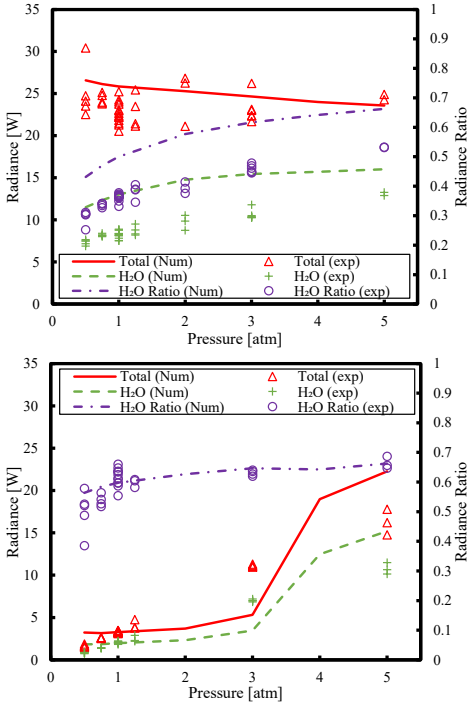


Figure 10: Experimental and numerical total radiance, H_2O radiance, and H_2O radiance ratio for (a) the point of peak hot flame radiance (experiments and computations) and (b) the point where the droplet diameter is 2.5 mm (experiments) and the point 10 s after hot flame extinction (computations).

outwards. As pressure increases above 3 atm the H_2O radiance remains constant, and the CO_2 radiance decreases slightly when reabsorption is included. The corresponding values for the optically thin cases increase with increasing pressure, once again demonstrating the strength of reabsorption in these flames.

The radiance ratios for CO_2 and H_2O in the cool flame are shown in Fig. 9b. In the optically thick calculations H_2O consistently contributes around 70% of the total radiance, while CO_2 contributes between 20% to 30%, with the contribution decreasing at higher pressures. This contrasts with the hot flame, where CO_2 radiance dominates with lower pressures. Since the cool flame starts after the warm/hot flame, reabsorption is high from the beginning due to large amounts of residual products. Additionally, CO_2 radiance is low due to its low production rate.

3.4 Experimental Comparison

Figure 10 compares the results obtained here with the results from microgravity droplet combustion experiments [16] for the hot, warm, and cool flames. In both the computations and the experiments, the hot flame points are taken at the point of peak hot flame radiance. The total radiance, H_2O radiance, and H_2O radiance ratio at this point are shown in Fig. 10a. For the warm and cool flames, experimentally the data was taken when the droplet diameter was 2.5 mm. Choosing this point results in cool flame data for pressures below 3 atm, and warm flame data for pressures of 3 atm and above. There is not a point in the calculations that directly correlates to a droplet diameter of 2.5 mm, so the point 10 s after hot flame extinction was chosen for comparison. This results in cool flames for pressures below 3 atm and warm flames for pressures of 4 atm and above. The total radiance, H_2O radiance, and H_2O radiance ratio at these points are shown in Fig. 10b.

For the hot flame, the total flame radiance shows little dependence on pressure experimentally and is roughly 25 W at all pressures. The numerical results show a slight decrease with increasing pressure, from 26.5 W to 23.5 W, as pressure increases from 0.5 to 5 atm. The difference in these trends is likely caused by the different boundary conditions for each configuration. The mass flow rate here is fixed, while in the experiments the burning rate increased slightly with increasing pressure [16]. The H_2O radiance increases with increasing pressure in both the experiments and simulations. The magnitude of the H_2O radiance is higher in the simulations compared to the experiments, likely owing to the limitations of the experimental hardware. The values from the

experiments are taken from a radiometer with a filter that only allows radiation in the 5-7 μm range to pass through, and the radiometer's response is not flat in this range [15]. Water vapor also emits radiation outside of this range, so it is expected that the measured magnitude would be less than the numerical predictions. The H_2O radiance ratio also increases with increasing pressure in both the experiments and simulations. The mechanism for this increased contribution from H_2O in the experiments is the same as was previously discussed for the simulations. The increasing pressure increases the molar concentrations and therefore the absorption coefficient, leading to larger amounts of CO_2 reabsorption compared to H_2O reabsorption.

For the cool and warm flames, the total radiance increases with increasing pressure in both the experiments and simulations. For the cool flames the increase is more pronounced in the experiments, while for the warm flames the increase is more pronounced in the simulations. These trends are the same for the H_2O radiance. The H_2O radiance ratio increases slightly with pressure in both the experiments and simulations and is in the same range for both.

4. Conclusions

The effects that ambient pressure had on radiance in simulations of microgravity burner-supported spherical diffusion flames were presented and compared to the results of microgravity droplet combustion experiments. Hot, warm, and cool flames were all considered. The main effect of increasing pressure was an increase in the reabsorption of radiation, particularly for CO_2, due to increased absorption coefficients. The main radiators throughout all three combustion regimes were CO_2 and H_2O, with CO never constituting more than 15% of the total radiance.

The contribution to total radiance shifted from CO_2 dominated to H_2O dominated as the flame burned and as pressure increased in the hot flame. In the warm and cool flames H_2O continued to contribute the majority of the radiance, and this contribution increased with increasing pressure. These trends, which were also observed experimentally, were not present when optically thin calculations were performed, i.e., when the radiation reabsorption term was removed from the radiative transfer equation.

This shift in radiation contributions was determined to be caused by the optically thick nature of the system. As absorption coefficient increased due to increased product concentrations, the CO_2 absorption band centered at 4.3 μm became easily saturated. This meant CO_2 radiance saw much lower increases as absorption coefficient increased compared to H_2O radiance. This result reinforces the notion that optically thin radiation models are unable to accurately capture the radiation behavior of high-pressure combustion systems.

CrediT authorship contribution statement

KAW: Formal analysis, Methodology, Software, Visualization, Writing – original draft, Writing – review & editing

DLD: Conceptualization, Investigation, Project administration, Writing – review & editing

VN: Writing – review and editing

Declaration of competing interest

The authors declare that they have no known competing financial interests or personal relationships that could have appeared to influence the work reported in this paper.

Acknowledgments

The authors would like to acknowledge the funding support of the NASA Postdoctoral Program and the Biological and Physical Sciences Division of NASA's Science Mission Directorate, and to thank Tim Krause for his efforts on experimental data collection and analysis.

References

[1] B.H. Chao, C.K. Law, J.S. T'ien, Structure and extinction of diffusion flames with flame radiation, Symp. (Int.) Combust. 23 (1991) 523–531.

[2] K. Mills, M. Matalon, Extinction of spherical diffusion flames in the presence of radiant loss, Symp. (Int.) Combust. 27 (1998) 2535–2541.

[3] V. Nayagam, D.L. Dietrich, M.C. Hicks, F.A. Williams, Radiative extinction of large n-alkane droplets in oxygen-inert mixtures in microgravity, Combust. Flame 194 (2018) 107–114.

[4] V. Nayagam, D.L. Dietrich, F.A. Williams, Radiative extinction of burner-supported spherical diffusion flames: A scaling analysis, Combust. Flame 205 (2019) 368–370.

[5] P.H. Irace, K.A. Waddell, D. Constales, P.B. Sunderland, R.L. Axelbaum, Critical temperature and reactant mass flux for radiative extinction of ethylene microgravity spherical diffusion flames at 1 bar, Proc. Combust. Inst. 39 (2023) 1905–1913.

[6] K.V. Liu, J.R. Lloyd, K.T. Yang, An investigation of a laminar diffusion flame adjacent to a vertical flat plate burner, Int. J. Heat Mass Transf. 24 (1981) 1959–1970.

[7] R. Viskanta, M.P. Mengüç, Radiation heat transfer in combustion systems, Prog. Energy Combust. Sci. 13 (1987) 97–160.

[8] A.J. Marchese, F.L. Dryer, The Effect of Non-Luminous Thermal Radiation in Microgravity Droplet Combustion, Combust. Sci. Technol. 124 (1997) 371–402.

[9] H. Bedir, J.S. T'ien, H.S. Lee, Comparison of different radiation treatments for a one-dimensional diffusion flame, Combust. Theory Model. 1 (1997) 395–404.

[10] H. Bedir, J.S. Tien, A computational study of flame radiation in PMMA diffusion flames including fuel vapor participation, Symp. (Int.) Combust. 27 (1998) 2821–2828.

[11] Y. Ju, H. Guo, F. Liu, K. Maruta, Effects of the Lewis number and radiative heat loss on the

bifurcation and extinction of CH_4 /O_2 -N_2 -He flames, J. Fluid Mech. 379 (1999) 165–190.
[12] J.L. Rhatigan, H. Bedir, J.S. T'ien, Gas-phase radiative effects on the burning and extinction of a solid fuel, Combust. Flame 112 (1998) 231–241.
[13] F. Liu, J.-L. Consalvi, P.J. Coelho, F. Andre, M. Gu, V. Solovjov, B.W. Webb, The impact of radiative heat transfer in combustion processes and its modeling – with a focus on turbulent flames, Fuel 281 (2020) 118555.
[14] H. Chu, M. Gu, J.-L. Consalvi, F. Liu, H. Zhou, Effects of total pressure on non-grey gas radiation transfer in oxy-fuel combustion using the LBL, SNB, SNBCK, WSGG, and FSCK methods, J. Quant. Spectrosc. Radiat. Transf. 172 (2016) 24–35.
[15] D.L. Dietrich, R. Calabria, P. Massoli, V. Nayagam, F.A. Williams, Experimental Observations of the Low-Temperature Burning of Decane/Hexanol Droplets in Microgravity, Combust. Sci. Technol. 189 (2017) 520–554.
[16] D. Dietrich, T. Krause, V. Nayagam, T. Farouk, F. Dryer, F. Williams, Low Temperature n-Dodecane Droplet Combustion Experiments Aboard the International Space Station, Microgravity Sci. Technol. 36 (2024) 31.
[17] A. Atreya, S. Agrawal, K. Sacksteder, H. Baum, Observations of methane and ethylene diffusion flames stabilized around a blowing porous sphere under microgravity conditions, 32nd Aerospace Sciences Meeting and Exhibit (1994).
[18] S.D. Tse, D. Zhu, C.-J. Sung, Y. Ju, C.K. Law, Microgravity burner-generated spherical diffusion flames: experiment and computation, Combust. Flame 125 (2001) 1265–1278.
[19] K.J. Santa, Z. Sun, B.H. Chao, P.B. Sunderland, R.L. Axelbaum, D.L. Urban, D.P. Stocker, Numerical and experimental observations of spherical diffusion flames, Combust. Theory Model. 11 (2007) 639–652.
[20] P.H. Irace, H.J. Lee, K. Waddell, L. Tan, D.P. Stocker, P.B. Sunderland, R.L. Axelbaum, Observations of long duration microgravity spherical diffusion flames aboard the International Space Station, Combust. Flame 229 (2021) 111373.
[21] V. Nayagam, D.L. Dietrich, P.V. Ferkul, M.C. Hicks, F.A. Williams, Can cool flames support quasi-steady alkane droplet burning?, Combust. Flame 159 (2012) 3583–3588.
[22] O.R. Yehia, C.B. Reuter, Y. Ju, Low-temperature multistage warm diffusion flames, Combust. Flame 195 (2018) 63–74.
[23] T.I. Farouk, D. Dietrich, F.L. Dryer, Three stage cool flame droplet burning behavior of n-alkane droplets at elevated pressure conditions: Hot, warm and cool flame, Proc. Combust. Inst. 37 (2019) 3353–3361.
[24] E. Lin, C.B. Reuter, Y. Ju, Dynamics and burning limits of near-limit hot, warm, and cool diffusion flames of dimethyl ether at elevated pressures, Proc. Combust. Inst. 37 (2019) 1791–1798.
[25] D.L. Dietrich, P.V. Ferkul, V.M. Bryg, M.V. Nayagam, M.C. Hicks, F.A. Williams, F.L. Dryer, B.D. Shaw, M.Y. Choi, C.T. Avedisian, Detailed Results From the Flame Extinguishment Experiment (FLEX) March 2009 to December 2011, NASA/TP-2015-216046, NASA Glenn Research Center, Cleveland, OH, 2015.
[26] D.L. Dietrich, V. Nayagam, M.C. Hicks, P.V. Ferkul, F.L. Dryer, T. Farouk, B.D. Shaw, H.K. Suh, M.Y. Choi, Y.C. Liu, C.T. Avedisian, F.A. Williams, Droplet Combustion Experiments Aboard the International Space Station, Microgravity Sci. Technol. 26 (2014) 65–76.
[27] S. Tang, M.K. Chernovsky, H.G. Im, A. Atreya, A computational study of spherical diffusion flames in microgravity with gas radiation Part I: Model development and validation, Combust. Flame 157 (2010) 118–126.
[28] V.R. Lecoustre, Numerical Investigations of Gaseous Spherical Diffusion Flames, PhD Dissertation, University of Maryland, 2009.
[29] R.J. Kee, J.F. Grcar, M.D. Smooke, J.A. Miller, E. Meeks, Premix: A FORTRAN Program for Modeling Steady Laminar One-Dimensional Premixed Flames, (1987).
[30] I.E. Gordon, L.S. Rothman, R.J. Hargreaves, R. Hashemi, E.V. Karlovets, F.M. Skinner, E.K. Conway, C. Hill, R.V. Kochanov, Y. Tan, P. Wcisło, A.A. Finenko, K. Nelson, P.F. Bernath, M. Birk, V. Boudon, A. Campargue, K.V. Chance, A. Coustenis, B.J. Drouin, et al., The HITRAN2020 molecular spectroscopic database, J. Quant. Spectrosc. Radiat. Transf. 277 (2022) 107949.
[31] J.C. Prince, F.A. Williams, Revised short mechanism for the low-temperature ignition of n-heptane for a wider pressure range, Fuel 150 (2015) 730–731.
[32] K.A. Waddell, D.L. Dietrich, V. Nayagam, Pressure effects in spherical microgravity hot, warm, and cool diffusion flame transitions, 14th U.S. National Combustion Meeting (2025), paper 2H05.